A 3DOF Path-Following Controller for a Non-Directionally Stable Vessel with Slow Thruster Dynamics

Emil H. Thyri * **Glenn Bitar** * **Morten Breivik** *

* *Centre for Autonomous Marine Operations and Systems (AMOS),*
Department of Engineering Cybernetics, Norwegian University of
Science and Technology (NTNU). NO-7491 Trondheim, Norway.
(e-mail: emil.h.thyri@ntnu.no,glennbitar@outlook.com,
morten.breivik@ieee.org)

Abstract: In this paper, a 3DOF path-following controller for an electric double-ended passenger ferry prototype is presented. The controller is formulated through a 3-step backstepping approach, taking into consideration several challenging physical properties of the vessel, such as a lack of passive damping in the vessel hull, lack of directional stability, and slow thruster dynamics compared to the vessel dynamics. The controller design also features a new thrust allocation approach that allows the thrust allocation of the over-actuated thruster system to be formulated on closed form, which enables us to include the thruster dynamics in the control law. The performance of the suggested 3DOF controller is demonstrated and compared to two other controllers through simulations with a model of the electric passenger ferry.

Keywords: 3DOF path-following control, non-directionally stable vessel, slow thruster dynamics, vectorial backstepping, thrust allocation.

1. INTRODUCTION

The motivation for the work presented in this paper is to develop a controller for the transit stage of a dock-to-dock operation for the milliAmpere vessel, which is an experimental platform for developing and testing technology for autonomous surface vessels. Three challenges with the physical properties of the vessel have been identified:

- The hull geometry of the milliAmpere vessel, which can be seen in Fig. 1, has a shallow draft and small length-to-beam ratio, makes it lack passive damping. This is particularly an issue in the sway and yaw mode. This manifests itself both in the lack of directional stability and in high sway velocity and thereby high sideslip angle when yawing.
- Inherent instability in yaw of the vessel's hull when the surge velocity exceeds about $1\,\text{m/s}$, where the forces on the hull act to turn the hull's broad-side towards the direction of travel. The mathematical interpretation of this is that when surging, the sideslip angle β has an unstable equilibrium at $\beta = 0$, and stable equilibriums at $\beta \sim \pm\pi/2$. The destabilizing yaw moment is increasing for increasing magnitude of β.
- The slow thruster dynamics of the vessel's two azimuth thrusters make it time-constrained fully actuated, despite being geometrically fully actuated. The dynamics of the azimuth angles have similar time constants to the dynamics of the vessel yaw angle, much due to the lack of passive damping. In combination with the yaw-instabilities, this makes the
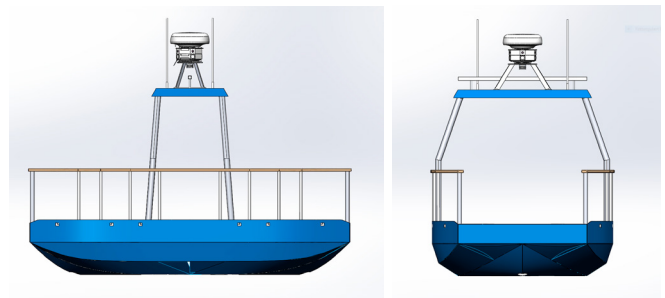

Fig. 1. Front and side view of the milliAmpere hull. The hull has a beam of $3\,\text{m}$ and a length of $5\,\text{m}$. Due to the small length-to-beam ratio, the shallow draft and the flat bottom, the vessel lacks directional stability and passive damping. This makes it highly maneuverable, but at the same time requires fast thruster dynamics for precise vessel control. Courtesy of Glenn Angell.

vessel heading hard to control at velocities exceeding $1\,\text{m/s}$.

In the controller presented in this paper, we therefore consider the listed problems in the controller design in an attempt to improve the performance. In addition to the controller design, a novel thrust allocation method is formulated, where a new set of control inputs puts the thrust allocation problem on closed form, in the sense that it is no longer underdetermined, and can be solved explicitly without optimization-based methods. The control law for the thruster setpoints are formulated through a backstepping method based on the one presented in (Khalil, 2013) and (Fossen, 2011). The proposed thrust

allocation allows us to include the thruster dynamics in the controller design.

Traditionally, 2 degrees of freedom (DOF) controllers have been used instead of 3DOF controllers when designing controllers for transit operations, both because most vessels are underactuated (at transit speed), and because fully actuated vessels have limited actuation effect in sway at high surge velocities. Extensive work has been done on this topic for sway-underactuated surface vessels, see (Pinkster and Nienhuis, 1986), (Lefeber et al., 2003), (Fossen et al., 2003), (Fossen, 2011) and (Eriksen and Breivik, 2017) and the references therein. A 2DOF approach, however, requires a hull with sufficient sway-yaw damping to control the vessel course through the heading. Additionally, a majority of the work does not consider the vessel actuators beyond the degree of actuation. They only consider the actuator geometry, i.e. geometrical placement, and typically not how long it takes for an actuator to obtain its desired force by rotating and/or changing RPM. For systems where the thruster dynamics is much faster than the vessel dynamics, neglecting the actuator dynamics is an acceptable simplification. For systems where this is not the case, neglecting the thruster dynamics can result in high allocation errors, poor tracking and instability. For such systems, the actuator dynamics should therefore be considered in the controller design.

The remainder of this paper is structured as follows: In Section 2, we introduce the vessel model. Section 3 describes the new thrust allocation approach. In Section 4, we present the controller design. Section 5 contains simulation results. Finally, Section 6 concludes the paper.

2. VESSEL MODELING

In the controller design, a 3DOF vessel model is applied, describing the vessel pose and velocity in the plane in a local NED frame (Fossen, 2011). The vessel states are given by the vectors $\boldsymbol{\eta} = [x, y, \psi]^T \in \Re^2 \times S$, which is the north and east position, and vessel heading, and $\boldsymbol{\nu} = [u, v, r]^T$, which is the body-fixed velocity in surge and sway, and yaw rate, respectively. In addition, the vessel has two azimuth thrusters positioned along the fore-aft centerline. The actuator states are the azimuth angles $\boldsymbol{\alpha} = [\alpha_f, \alpha_a]^T \in S^2$ and the propeller RPMs $\boldsymbol{\omega} = [\omega_f, \omega_a]^T \in \Re^2$, where subscripts f and a refer to the fore and aft thruster, respectively.

The ship's dynamics from Fossen (2011) are given by

$$\dot{\boldsymbol{\eta}} = \mathbf{R}(\psi)\boldsymbol{\nu}, \qquad (1)$$

$$\mathbf{M}\dot{\boldsymbol{\nu}} + \mathbf{C}(\boldsymbol{\nu})\boldsymbol{\nu} + \mathbf{D}(\boldsymbol{\nu})\boldsymbol{\nu} = \boldsymbol{\tau}(\boldsymbol{\alpha}, \boldsymbol{\omega}), \qquad (2)$$

where $\mathbf{R}(\psi)$ represents the principal rotation around the z-axis

$$\mathbf{R}(\psi) = \begin{bmatrix} \cos\psi & -\sin\psi & 0 \\ \sin\psi & \cos\psi & 0 \\ 0 & 0 & 1 \end{bmatrix}, \qquad (3)$$

$\mathbf{M}$ is the inertia matrix including hydrodynamically added mass

$$\mathbf{M} = \begin{bmatrix} m_{11} & 0 & 0 \\ 0 & m_{22} & m_{23} \\ 0 & m_{32} & m_{33} \end{bmatrix}, \qquad (4)$$

$\mathbf{C}(\boldsymbol{\nu})$ is the Coriolis-centripetal matrix

$$\mathbf{C}(\boldsymbol{\nu}) = \begin{bmatrix} 0 & 0 & c_{13}(v, r) \\ 0 & 0 & c_{23}(u) \\ -c_{13}(v, r) & -c_{23}(u) & 0 \end{bmatrix}, \qquad (5)$$

and $\mathbf{D}(\boldsymbol{\nu})$ is the damping matrix

$$\mathbf{D}(\boldsymbol{\nu}) = \begin{bmatrix} d_{11}(u) & 0 & 0 \\ 0 & d_{22}(v, r) & d_{23}(u, v, r) \\ 0 & d_{32}(u, v, r) & d_{33}(u, v, r) \end{bmatrix}, \qquad (6)$$

The generalized force produced by the thrusters is given by

$$\boldsymbol{\tau}(\boldsymbol{\alpha}, \boldsymbol{\omega}) = \begin{bmatrix} \Phi(\omega_f)\cos\alpha_f + \Phi(\omega_a)\cos\alpha_a \\ \Phi(\omega_f)\sin\alpha_f + \Phi(\omega_a)\sin\alpha_a \\ l_f\Phi(\omega_f)\sin\alpha_f + l_a\Phi(\omega_a)\sin\alpha_a \end{bmatrix}, \qquad (7)$$

where the function $\Phi(\omega_i)$ is fitted to bollard-pull data, and maps the propeller rotational velocity to a force, and l_f and l_a are lengths from the ship's body origin to the fore and aft thruster respectively. Since milliAmpere is fore-aft symmetric, $l_f = -l_a$.

The model for the thruster azimuth angle and propeller dynamics are

$$\dot{\alpha}_i = \frac{K_{i,\alpha}(\alpha_{i,d} - \alpha_i)}{\sqrt{(\alpha_{i,d} - \alpha_i)^2 + \epsilon_i^2}}, \qquad (8)$$

$$\dot{\omega}_i = K_{i,\omega}(\omega_{i,d} - \omega_i), \qquad (9)$$

where $K_{i,\alpha} > 0$, $\epsilon_i > 0$ and $K_{i,\omega} > 0$ for $i \in \{f, a\}$. All model parameters are determined through the work done by Pedersen (2019), where an optimization-based approach to system identification from experimental data is applied. Conversion of units for $K_{i,\alpha}$ and ϵ_i is necessary since they were estimated in degrees, and we use radians. That is, $K_{i,\alpha} = \frac{\pi}{180°}K_{i,\alpha}^*$ and $\epsilon_i = \frac{\pi}{180°}\epsilon_i^*$, where the starred variables are the numerical values given in (Pedersen, 2019).

3. THRUST ALLOCATION

Since the vessel has four control inputs and is overactuated, the thrust allocation is not trivial. The authors of (Johansen and Fossen, 2013) give a thorough survey of existing methods for thrust allocation for over-actuated systems by means of optimization-based algorithms, where a generalized force can be realized by an arbitrary number of actuators. The actuator setpoints are optimized with respect to objectives such as minimal wear and tear or energy consumption. Such methods are suitable when the dynamics of the thrusters relative to the system are fast enough that they can be omitted in the controller design. If this is not the case, and the thruster and vessel dynamics have comparable time constants, the thruster dynamics must be considered in the controller design.

As mentioned, this is the case for the milliAmpere, which we demonstrate through the introduction of the time-to-actuation (TTA) metric. We define this as the time it takes from thruster setpoints are set and until the normalized allocation errors

$$\tilde{X} = \frac{X - X_d}{X_d}, \qquad (10)$$

$$\tilde{Y} = \frac{Y - Y_d}{Y_d}, \qquad (11)$$

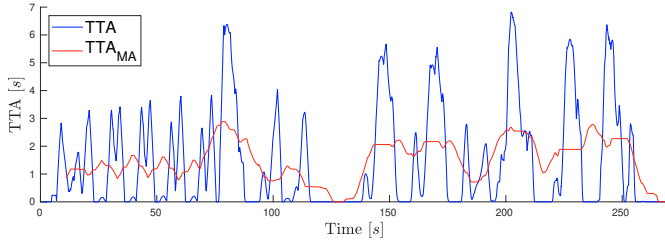$$\tilde{N} = \frac{N - N_d}{N_d}, \qquad (12)$$

Fig. 2. Simulated TTA and moving average over 20 s, TTA_{MA}.

are less than 15%, where X_d and Y_d are the desired surge and sway forces respectively, and N_d is the desired sway moment corresponding to the thruster setpoints. The TTA is determined by simulating the thruster states from the configuration they are in when the setpoints are set. The TTA is shown in Fig. 2 for a simulated transit. The figure shows the TTA and a moving average of the TTA over a 20 s interval, denoted TTA_{MA}. From the graph, we can see that it takes the thrusters on average more than two seconds to realize $\boldsymbol{\tau}_d$ for parts of the transit. In an equal amount of time the milliAmpere can yaw close to 90° by a yaw moment from its thrusters, or around 45° by a sudden gust of wind. This advocates considering the thruster dynamics when formulating a control law for this vessel.

To do this, we propose a method where first the thrust allocation is simplified and formulated on closed form, and subsequently the thruster dynamics are included as part of the controller design. The input space is thus reduced from $\Re^2 \times S^2$ to $\Re \times S^2$ by the introduction of a new desired state vector

$$\boldsymbol{\rho}_d := [F_d, \alpha_d, \gamma_d]^\mathsf{T} \qquad (13)$$

with a corresponding state vector

$$\boldsymbol{\rho} := [F, \alpha, \gamma]^\mathsf{T}. \qquad (14)$$

This mapping is physically intuitive, where F is the total force produced by the thrusters, and the angles α and γ actuate the yaw moment and sway force respectively. The relationship between the new thruster states and the original thruster states is illustrated in Fig. 3.

The mapping from the new reduced set of thruster states $\boldsymbol{\rho}$ to the thruster states $\boldsymbol{\omega} = [\omega_f, \omega_a]^\mathsf{T}$ and $\boldsymbol{\alpha} = [\alpha_f, \alpha_a]^\mathsf{T}$ is given by

$$\begin{bmatrix} \omega_f \\ \omega_a \\ \alpha_f \\ \alpha_a \end{bmatrix} = \begin{bmatrix} \Omega(\frac{F}{2}) \\ \Omega(\frac{F}{2}) \\ \alpha + \gamma \\ -\alpha + \gamma \end{bmatrix}, \qquad (15)$$

where the force F is split equally between the fore and aft thrusters. The function $\Omega(F)$ is the inverse of $\Phi(\omega)$, and maps a force to the corresponding rotational velocity of the propeller. The mapping from $\boldsymbol{\rho}$ to the generalized force is then

$$\boldsymbol{\tau} = \begin{bmatrix} F \cos\alpha \cos\gamma \\ F \cos\alpha \sin\gamma \\ lF \sin\alpha \cos\gamma \end{bmatrix}. \qquad (16)$$

This new input space reduces the number of control input variables in the thrusters from 4 to 3 by assigning equal thrust to both thrusters. This restricts the theoretical performance of the thruster system, however, it allows us to formulate the thrust allocation problem on closed form,
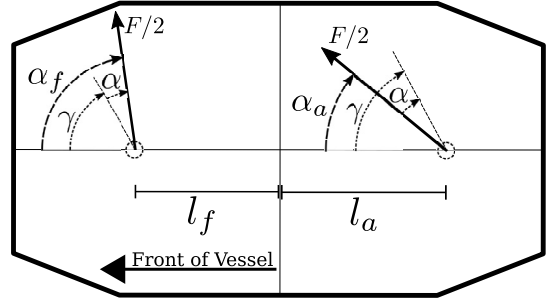

Fig. 3. Thruster configuration of the milliAmpere. Relationship between the new thruster states α and γ, and α_f and α_a are indicated.

which enables us to consider the thruster dynamics in the controller design.

From a desired force vector $\boldsymbol{\tau}_d = [X_d, Y_d, N_d]^\mathsf{T}$, the mapping to the control variables $\boldsymbol{\rho}_d$ is

$$\boldsymbol{\rho}_d = \begin{bmatrix} 1/(lX_d)\sqrt{X_d^4 l^2 + X_d^2 Y_d^2 l^2 + X_d^2 N_d^2 + Y_d^2 N_d^2} \\ \text{atan2}(N_d, lX_d) \\ \text{atan2}(Y_d, X_d) \end{bmatrix}. \qquad (17)$$

In the mapping (17), the following assumptions are applied:

Assumption 1. X_d is always positive.

Assumption 2. The force X_d is large enough in relation to both Y_d and N_d such that the sum of the absolute value of the angles α_d and γ_d are always less than $\pi/2$.

Since the controller is intended for transit, where the major component of the velocity will be in the surge direction, the first assumption is ensured. The proposed controller is hence not suitable for station-keeping operations, and the controller will have to be paired with one suitable for low-speed, station-keeping and docking operations for a full dock-to-dock operation. The second assumption is more restrictive since it puts limitations on the reference signals in sway and yaw, in addition to limiting the magnitude of environmental forces the vessel can handle for a given surge velocity. Yet, at transit velocities, the X component should be sufficiently large to ensure the assumption holds for reasonable yaw rates and environmental disturbances.

3.1 New thruster state dynamics

To include the thruster dynamics in the controller design, a dynamic model for the new thruster states that is affine in the control input $\boldsymbol{\rho}_d$ is needed. There is no trivial way to formulate the dynamics of F, α and γ on an affine form in terms of the dynamics of (8) and (9), since $\Omega(.)$ is a nonlinear lookup-table based on bollard-pull data, and the dynamics of the azimuth angle is a nonlinear function in both α and γ. We therefore chose to model the new thruster states as first-order systems with suitable time constants, with

$$\dot{F} = \frac{1}{T_F}(F_d - F), \qquad (18)$$

where the time constant is chosen to be the same as for the propeller dynamics, namely $T_F = 1/K_{i,\alpha}$, and

$$\dot{\alpha} = \frac{1}{T_\alpha}(\alpha_d - \alpha), \qquad (19)$$
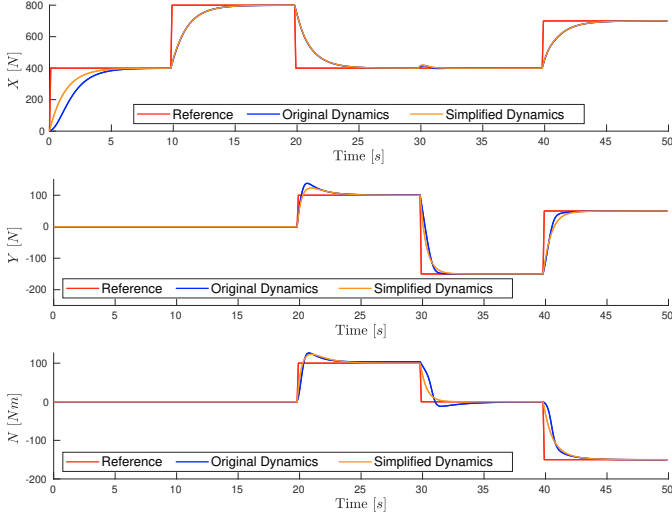
Fig. 4. Comparison of the original thruster dynamics in (8) and (9), and the proposed simplified thruster dynamics in (21).

$$\dot{\gamma} = \frac{1}{T_\gamma}(\gamma_d - \gamma), \tag{20}$$

where the choice of time constants need to consider the slow dynamics of the azimuth angle.

This puts the new thruster state dynamics on the form,

$$\dot{\boldsymbol{\rho}} = \boldsymbol{K}_T(\boldsymbol{\rho}_d - \boldsymbol{\rho}), \tag{21}$$

where $\boldsymbol{K}_T = diag(1/T_F, 1/T_\alpha, 1/T_\gamma)$ and $\boldsymbol{K}_T > 0$.

In Fig. 4, the simplified thruster dynamics and the original thruster dynamics are compared. For the dynamics (8) and (9), the setpoints are found by the thrust allocation method from (Torben et al., 2019). For the dynamics in (21), the setpoints are found by (17). The deviation in X for low magnitudes arise because the thrusters have a deadband at low propeller RPM which is considered in $\Phi(.)$ but not in (18).

4. CONTROLLER DESIGN

In this section, the 3DOF path-following controller is formulated through a 3-step backstepping approach, where the final step includes the dynamics of the newly introduced thruster states in the closed-form thrust allocation. The controller design is made based on the following state-space system where $\boldsymbol{x}$ is the integral of the velocity, and $\boldsymbol{\rho}_d$ is the control input,

$$\dot{\boldsymbol{x}} = \boldsymbol{\nu}, \tag{22}$$

$$\boldsymbol{M}\dot{\boldsymbol{\nu}} + \boldsymbol{C}(\boldsymbol{\nu})\boldsymbol{\nu} + \boldsymbol{D}(\boldsymbol{\nu})\boldsymbol{\nu} = \boldsymbol{\tau}(\boldsymbol{\rho}, \boldsymbol{\rho}_d), \tag{23}$$

$$\dot{\boldsymbol{\tau}}(\boldsymbol{\rho}, \boldsymbol{\rho}_d) = \boldsymbol{B}(\boldsymbol{\rho})\boldsymbol{K}_T(\boldsymbol{\rho}_d - \boldsymbol{\rho}), \tag{24}$$

with

$$\boldsymbol{B}(\boldsymbol{\rho}) = \begin{bmatrix} c(\alpha)c(\gamma) & -Fs(\alpha)c(\gamma) & -Fc(\alpha)s(\gamma) \\ s(\gamma)c(\alpha) & -Fs(\gamma)c(\alpha) & Fc(\gamma)c(\alpha) \\ ls(\alpha)c(\gamma) & Flc(\alpha)c(\gamma) & -Fls(\alpha)s(\gamma) \end{bmatrix}, \tag{25}$$

where $\boldsymbol{B}(\boldsymbol{\rho})$ is the time derivative of (16) with respect to $\boldsymbol{\rho}$, and $s(.)$ and $c(.)$ are the sine and cosine function respectively.

4.1 Backstepping

Step 1 First, we consider the dynamics of $\tilde{\boldsymbol{x}}$, which is the integral of the velocity error $\tilde{\boldsymbol{\nu}} = \boldsymbol{\nu} - \boldsymbol{\nu}_d$, where $\boldsymbol{\nu}_d \in \Re^3$ is the desired body-fixed velocity vector. Hence, $\tilde{\boldsymbol{x}}$ holds the integral error of the surge and sway velocity, and the heading error. By including integral effects, steady-state disturbances can be compensated for. For $\tilde{\boldsymbol{x}}$, we consider $\boldsymbol{\nu}$ as the control input. Then, let

$$\boldsymbol{\nu} = \boldsymbol{z}_1 + \boldsymbol{\alpha}_1, \tag{26}$$

where $\boldsymbol{\alpha}_1$ is a stabilizing vector that will be defined shortly, and $\boldsymbol{z}_1 = \boldsymbol{\nu} - \boldsymbol{\alpha}_1$ is a new state variable. The dynamics of $\tilde{\boldsymbol{x}}$ can then be written as

$$\begin{aligned} \dot{\tilde{\boldsymbol{x}}} &= \boldsymbol{\nu} - \boldsymbol{\nu}_d \\ &= \boldsymbol{z}_1 + \boldsymbol{\alpha}_1 - \boldsymbol{\nu}_d. \end{aligned} \tag{27}$$

A control Lyapunov function (CLF) is formulated as

$$V_1 = \frac{1}{2}\tilde{\boldsymbol{x}}^\mathsf{T}\tilde{\boldsymbol{x}}, \tag{28}$$

with the time derivative

$$\dot{V}_1 = \tilde{\boldsymbol{x}}^\mathsf{T}(\boldsymbol{z}_1 + \boldsymbol{\alpha}_1 - \boldsymbol{\nu}_d). \tag{29}$$

The vector field $\boldsymbol{\alpha}_1$ can then be designed to stabilize the dynamics of $\tilde{\boldsymbol{x}}$. We define it as

$$\boldsymbol{\alpha}_1 := \boldsymbol{\nu}_d - \boldsymbol{K}_p\tilde{\boldsymbol{x}}, \tag{30}$$

with $\boldsymbol{K}_p = \boldsymbol{K}_p^\mathsf{T} > 0$. This gives the state dynamics

$$\dot{\tilde{\boldsymbol{x}}} = -\boldsymbol{K}_p\tilde{\boldsymbol{x}} + \boldsymbol{z}_1, \tag{31}$$

and the CLF derivative

$$\begin{aligned} \dot{V}_1 &= \tilde{\boldsymbol{x}}^\mathsf{T}(-\boldsymbol{K}_p\tilde{\boldsymbol{x}} + \boldsymbol{z}_1) \\ &= -\tilde{\boldsymbol{x}}^\mathsf{T}\boldsymbol{K}_p\tilde{\boldsymbol{x}} + \boldsymbol{z}_1^\mathsf{T}\tilde{\boldsymbol{x}}. \end{aligned} \tag{32}$$

Here, $\dot{V}_1 < 0 \ \forall \tilde{\boldsymbol{x}} \in \Re^3 \notin \{\boldsymbol{0}\}$ if $\boldsymbol{z}_1 = \boldsymbol{0}$, hence the $\tilde{\boldsymbol{x}} = \boldsymbol{0}$ is UGAS if $\boldsymbol{z}_1 = \boldsymbol{0}$.

Step 2 We now address the new state $\boldsymbol{z}_1$. An augmented CLF with the pseudo-kinetic energy of the system is formulated as

$$V_2 = \frac{1}{2}\boldsymbol{z}_1\boldsymbol{M}\boldsymbol{z}_1 + V_1, \tag{33}$$

where $\boldsymbol{M} > 0$ is the inertia matrix.

The CLF time derivative is

$$\begin{aligned} \dot{V}_2 &= \boldsymbol{z}_1\boldsymbol{M}\dot{\boldsymbol{z}}_1 + \dot{V}_1 \\ &= \boldsymbol{z}_1[\boldsymbol{\tau}(\boldsymbol{\rho}, \boldsymbol{\rho}_d) - \boldsymbol{M}\dot{\boldsymbol{\alpha}}_1 - (\boldsymbol{C}(\boldsymbol{\nu}) + \boldsymbol{D}(\boldsymbol{\nu}))\boldsymbol{\alpha}_1 \\ &\quad - (\boldsymbol{C}(\boldsymbol{\nu}) + \boldsymbol{D}(\boldsymbol{\nu}))\boldsymbol{z}_1] - \tilde{\boldsymbol{x}}^\mathsf{T}\boldsymbol{K}_p\tilde{\boldsymbol{x}} + \boldsymbol{z}_1^\mathsf{T}\tilde{\boldsymbol{x}} \\ &= \boldsymbol{z}_1[\boldsymbol{\tau}(\boldsymbol{\rho}, \boldsymbol{\rho}_d) - \boldsymbol{M}\dot{\boldsymbol{\alpha}}_1 - (\boldsymbol{C}(\boldsymbol{\nu}) + \boldsymbol{D}(\boldsymbol{\nu}))\boldsymbol{\alpha}_1) \\ &\quad - (\boldsymbol{C}(\boldsymbol{\nu}) + \boldsymbol{D}(\boldsymbol{\nu}))\boldsymbol{z}_1 + \tilde{\boldsymbol{x}}] - \tilde{\boldsymbol{x}}^\mathsf{T}\boldsymbol{K}_p\tilde{\boldsymbol{x}}. \end{aligned} \tag{34}$$

The generalized force $\boldsymbol{\tau}(\boldsymbol{\rho}, \boldsymbol{\rho}_d)$ can now be considered as the control input, and

$$\boldsymbol{\tau}(\boldsymbol{\rho}, \boldsymbol{\rho}_d) = \boldsymbol{z}_2 + \boldsymbol{\alpha}_2, \tag{35}$$

where $\boldsymbol{z}_2$ is a new state variable and $\boldsymbol{\alpha}_2$ is a stabilizing vector that can be designed to stabilize $\boldsymbol{z}_1$, that we define as

$$\boldsymbol{\alpha}_2 := \boldsymbol{M}\dot{\boldsymbol{\alpha}}_1 + (\boldsymbol{C}(\boldsymbol{\nu}) + \boldsymbol{D}(\boldsymbol{\nu}))\boldsymbol{\alpha}_1 - \tilde{\boldsymbol{x}} - \boldsymbol{K}_d\boldsymbol{z}_1 \tag{36}$$

with $\boldsymbol{K}_d = \boldsymbol{K}_d^\mathsf{T} > 0$. By appropriate selection of the entries in $\boldsymbol{K}_d$, the low passive damping in sway and yaw can be compensated for. The choice of $\boldsymbol{\alpha}_2$ gives the new state dynamics

$$\dot{\boldsymbol{z}}_1 = -(\boldsymbol{C}(\boldsymbol{\nu}) + \boldsymbol{D}(\boldsymbol{\nu}) + \boldsymbol{K}_d)\boldsymbol{z}_1 - \tilde{\boldsymbol{x}} + \boldsymbol{z}_2, \tag{37}$$

and the CLF derivative

$$\dot{V}_2 = z_1^\top z_2 - z_1(C(\nu) + D(\nu) + K_d)z_1 - \tilde{x}^\top K_p \tilde{x}, \quad (38)$$

which is negative definite and hence UGAS in $\tilde{x} = 0$ and $z_1 = 0$ if $z_2 = 0$.

Step 3 Finally, the new state z_2 is addressed. A further augmented CLF is defined as

$$V_3 := \frac{1}{2}z_2^\top z_2 + V_2 \quad (39)$$

with the time derivative

$$\begin{aligned}
\dot{V}_3 &= z_2^\top \dot{z}_2 + \dot{V}_2, \\
&= z_2^\top(\dot{\tau}(\rho, \rho_d) - \dot{\alpha}_2) + z_1^\top z_2 \\
&\quad - z_1(C(\nu) + D(\nu) + K_d)z_1 - \tilde{x}^\top K_p \tilde{x}, \quad (40) \\
&= z_2^\top(B(\rho)K_T(\rho_d - \rho) - \dot{\alpha}_2 + z_1) \\
&\quad - z_1(C(\nu) + D(\nu) + K_d)z_1 - \tilde{x}^\top K_p \tilde{x}.
\end{aligned}$$

Here, we note that ρ_d, which is the control input to the system (22)-(24), finally appears in the CLF derivative. A control law can then be formulated for ρ_d to ensure a negative definite $\dot{V}_3$. We define the control law:

$$\rho_d := \rho + K_T^{-1}B(\rho)^{-1}(\dot{\alpha}_2 - z_1 - K_{z_2}z_2), \quad (41)$$

where $K_{z_2} = K_{z_2}^\top > 0$. The state derivative then becomes

$$\dot{z}_2 = -z_1 - K_{z_2}z_2, \quad (42)$$

and the CLF derivative becomes

$$\begin{aligned}
\dot{V}_3 = &- z_2^\top K_{z_2}z_2 - z_1^\top(C(\nu) + D(\nu) + K_d)z_1 \\
&- \tilde{x}^\top K_p \tilde{x}, \quad (43)
\end{aligned}$$

where $\dot{V}_3 < 0 \ \forall \ \tilde{x}, z_1, z_2 \in \Re^3 \notin \{0\}$ if $(C(\nu) + D(\nu) + K_d) > 0 \ \forall \nu \in \Re^3$, and hence $\tilde{x} = 0$, $z_1 = 0$, $z_2 = 0$ is UGAS for the control law (41), given that the system is as modelled in (1)-(9) and that the approximation of the thruster dynamics is accurate, which is indicated in Fig. 4.

In (41), we assume that the matrix $B(\rho)$ is non-singular and hence invertible. This is not guaranteed in itself, since $B(\rho)$ is singular if at least one of the following is true;

(a) $F = 0$,
(b) $\alpha = \pm\pi/2$,
(c) $\gamma = \pm\pi/2$.

However (a) is covered by Assumption 1, while (b) and (c) are considered by Assumption 2.

5. SIMULATION RESULTS

In this section, we present simulation results for the proposed control law in (41). In the simulations, the vessel GNC system inputs a set of waypoints with corresponding speed references, while a LOS guidance law with constant lookahead distance calculates the heading reference (Fossen et al., 2003). The speed and heading references are passed through second and third order reference filters, respectively, to get continuous acceleration and jerk references.

Simulation results are presented for a transit along a path as shown in Fig. 5, where the reference path from the waypoints is illustrated in red, and the path taken by the vessel with the proposed 3DOF controller is blue. The simulations are run with a constant disturbance in the NED frame, with a magnitude of 100 N in the direction

Table 1. Control parameters

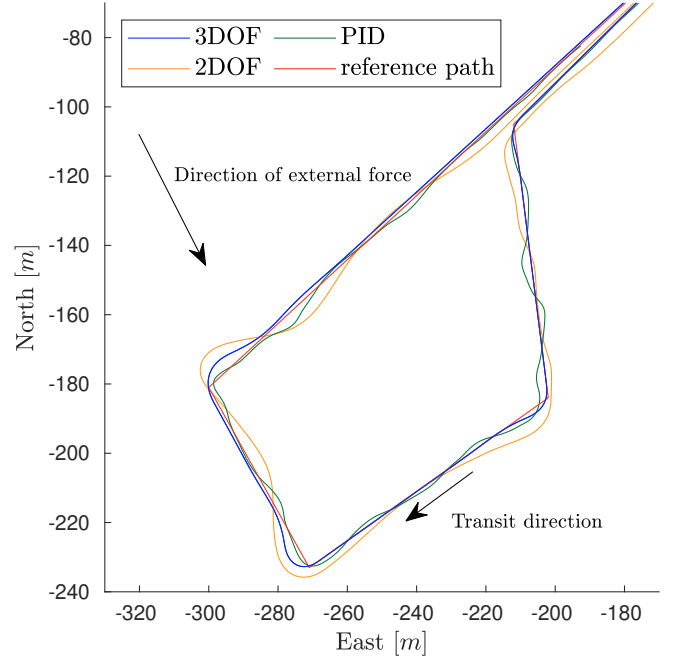| Parameter	Value	Unit
K_T	diag(1.78,2,2)	[s,s,s]
K_p	diag(3,1,5)	[1/s,1/s,1/s]
K_d	diag(1,1,1)	[kg/s,kg/s,kgm/s]
K_{z_2}	diag(5,10,5)	[1/kg,1/kg,1/kgm]

Fig. 5. Transit path from waypoints, and paths taken by the vessel. The direction of travel along the path, and direction of external forces are indicated by arrows.
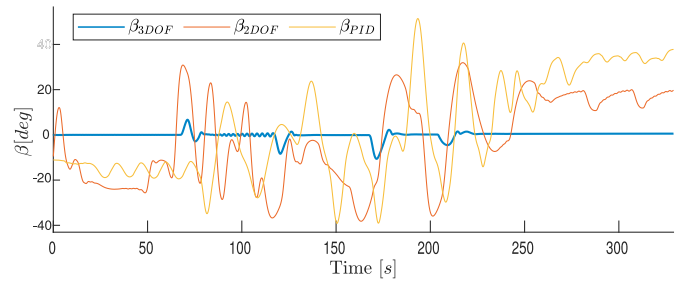

Fig. 6. Sideslip angle for the three controllers.

of the largest arrow in the figure. In addition to the results from the proposed controller, the transit path and sideslip angle from two other controllers are included for comparison:

- A 2DOF path-following controller designed through backstepping with thruster dynamics and thruster inputs F_d and α_d but not γ_d. The controller is augmented with an integrator on the course error to compensate for sideslip.
- A PID controller with velocity and acceleration feedforward, and the thrust allocation proposed by Torben et al. (2019).

The vessel path in Fig. 5 shows that the vessel tracks the reference path with satisfactory precision, where the cross-track error close to each waypoint is a consequence
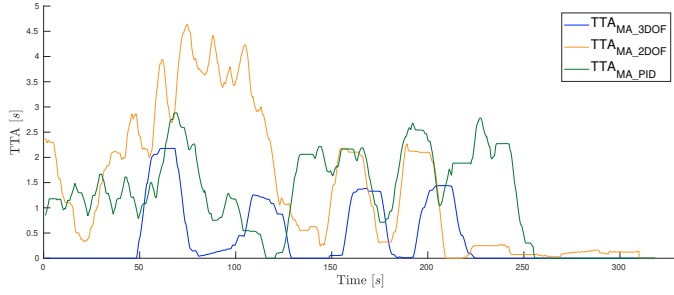
Fig. 7. Moving average over 20 s of time-to-actuation for the three controllers.
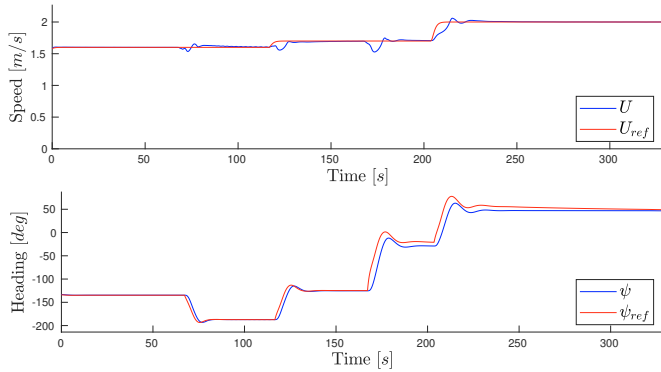
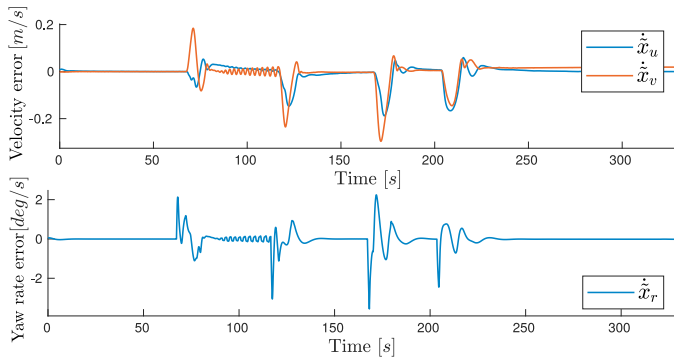

Fig. 8. Speed and heading, with references.

Fig. 9. Velocity error in surge and sway, and yaw rate error.

of the LOS guidance approach. From the figure, one can see that both the 2DOF controller and the PID controller track the path with comparable precision, but with more fluctuations about the reference path. This gives both high yawing and high sway velocities, as can be seen from the slip angle in Fig. 6, which, in turn, results in high derivatives in the actuator setpoints. The result of this is apparent from Fig. 7, where the TTA_{MA} is shown for the three controllers. High fluctuations in heading gives a high TTA, and hence high allocation error. This is most apparent for the 2DOF controller, where the heading is used to compensate for sway velocity, which is inefficient due to the lack of directional stability, and gives oscillations due to heading instability.

From Fig. 8, one can see that both the speed and heading reference is tracked with precision, where steady-state velocity errors resulting from external forces are compensated for by the integrator states in $\tilde{\boldsymbol{x}}$. From the graph of
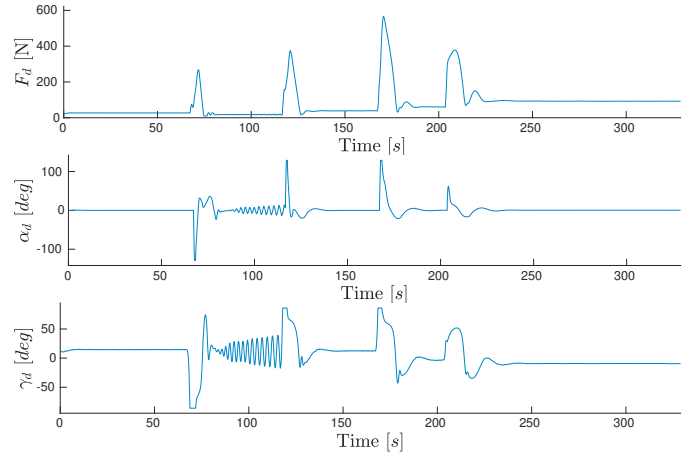

Fig. 10. Control inputs $\boldsymbol{\rho}_d$ for the 3DOF controller.

$\dot{\tilde{\boldsymbol{x}}}$ in Fig. 9, one can see that the sway velocity error is kept low, and hence, the sway velocity close to its reference at 0 m/s during turning maneuvers. This keeps the sideslip angle β low, and thereby the destabilizing yaw moment low. This reduces the need for excessive actuator rate changes, which is apparent from Fig. 7, where the proposed 3DOF controller has the lowest TTA_{MA}.

On the second leg of the path, the vessel course is the most aligned with the direction of the external forces. This gives a low F_d due to the contribution of the external force to the surge velocity. In turn, this results in high α_d and γ_d control inputs to compensate for small tracking errors in yaw rate and sway velocity, respectively. These unstable tendencies are a result of Assumption 2 being challenged, and they demonstrate how the control allocation approach
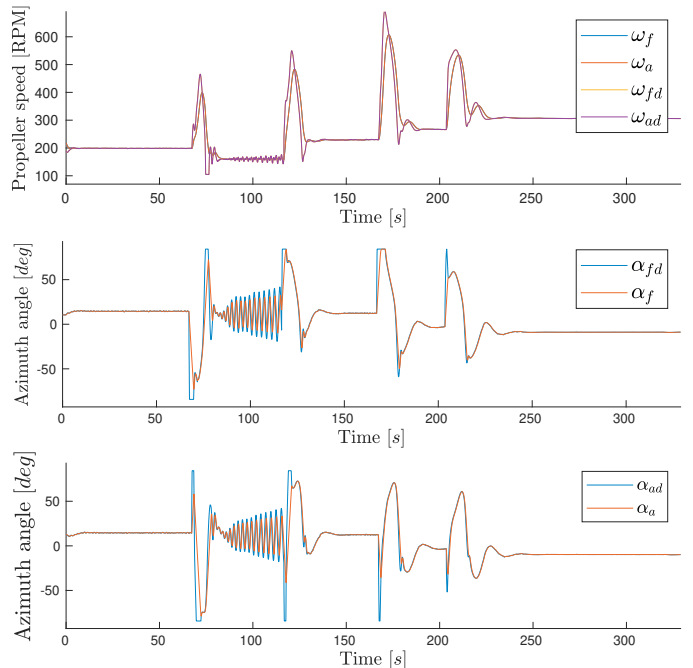

Fig. 11. Desired and actual thruster states. Due to the control allocation, ω_{fd} and ω_{ad} are superimposed.

can be restricted by the relationship between surge velocity and environmental forces.

From Fig. 11, one can see that the thruster angles α_{fd} and α_{ad} go into saturation during several of the turning maneuvers because the maneuver requires high actuation of both the sway and yaw mode simultaneously. This is another indication that Assumption 2 is being challenged, with a too small turning radius for the given surge velocity. This can be mitigated by increasing the lookahead distance, albeit at the cost of increased tracking error around the waypoints, or by a more suitable guidance method.

6. CONCLUSIONS AND FUTURE WORK

The development of a 3DOF path-following controller for a double-ended passenger ferry through a 3-step backstepping approach has been presented. The controller design is motivated by inherent issues with the physical properties of the ferry, where the lack of passive damping in sway is accounted for by active control of the sway velocity. This, in turn, reduces the effect of an inherent instability in yaw. A set of new thruster states is applied to reduce the actuator input space to be able to formulate the thrust allocation on closed form. Slow actuator dynamics are accounted for by including a simplified model of the actuator dynamics in the controller design, and thereby mitigating the erroneous assumption that the allocation error is sufficiently small to be neglected. The 3DOF controller is tested in numerical simulations, and compared to two other controllers. The proposed controller performs path following with satisfactory precision, and its performance is significantly better than the other controllers.

Future work include full-scale experiments and testing, in addition to further work on the thrust allocation to develop a hybrid system that can handle both low-speed docking and station-keeping operations as well as high-speed transit.

ACKNOWLEDGEMENTS

REFERENCES

Eriksen, B.O.H. and Breivik, M. (2017). *Modeling, Identification and Control of High-Speed ASVs: Theory and Experiments*, 407–431. Springer International Publishing, Cham. doi:10.1007/978-3-319-55372-6_19. URL https://doi.org/10.1007/978-3-319-55372-6_19.

Fossen, T.I. (2011). *Handbook of Marine Craft Hydrodynamics and Motion Control*. John Wiley & Sons.

Fossen, T.I., Breivik, M., and Skjetne, R. (2003). Line-of-sight path following of underactuated marine craft. *IFAC Proceedings Volumes*, 36(21), 211 – 216. doi: https://doi.org/10.1016/S1474-6670(17)37809-6. 6th IFAC Conference on Manoeuvring and Control of Marine Craft (MCMC 2003), Girona, Spain, 17-19 September.

Johansen, T.A. and Fossen, T.I. (2013). Control allocation-A survey. *Automatica*, 49(5), 1087 – 1103. doi:https://doi.org/10.1016/j.automatica.2013.01.035.

Khalil, H.K. (2013). *Nonlinear Systems*. Pearson Education Limited.

Lefeber, E., Pettersen, K.Y., and Nijmeijer, H. (2003). Tracking control of an underactuated ship. *IEEE Transactions on Control Systems Technology*, 11(1), 52–61. doi:10.1109/TCST.2002.806465.

Pedersen, A.A. (2019). *Optimization Based System Identification for the milliAmpere Ferry*. Master's thesis, Norwegian University of Science and Technology (NTNU), Trondheim, Norway.

Pinkster, J. and Nienhuis, U. (1986). Dynamic Positioning of Large Tankers at Sea. In *Proc. 18th Annual Offshore Technology Conference*, 459–476. Houston, Texas.

Torben, T.R., Brodtkorb, A.H., and Sørensen, A.J. (2019). Control allocation for double-ended ferries with full-scale experimental results. *IFAC-PapersOnLine*, 52(21), 45–50. doi:https://doi.org/10.1016/j.ifacol.2019.12.281. 12th IFAC Conference on Control Applications in Marine Systems, Robotics, and Vehicles (CAMS 2019), Daejeon, South Korea.